PCCP

ROYAL SOCIETY OF CHEMISTRY

PAPER

View Article Online
View Journal | View Issue

Cite this: *Phys. Chem. Chem. Phys.*, 2026, **28**, 1207

Photochemical transformation of weakly absorbing organics by visible light in microdroplets

Alexander Logozzo[a] and Thomas C. Preston *[ab]

Microdroplets provide a solute environment where concentrations readily surpass bulk saturation limits. How this persistent supersaturation influences reaction rates and photochemical pathways remains largely unexplored. Here, we investigate photochemical transformations of six "non-absorbing" organic molecules (glycine, proline, serine, glucose, ribose, and deoxyribose) in single aqueous microdroplets using optical trapping at two different laser wavelengths (473 and 532 nm). The contact-free environment allows for the suspension of supersaturated microdroplets, similar to those observed in natural aerosol particles in the atmosphere. In microdroplets containing water and the organic species, we observed photochemical transformations at optical wavelengths for all solutes. The organic molecules considered here are typically known to absorb light in the UV range, specifically at wavelengths no longer than 200 nm. The observed timescales for these photochemical reactions scale with the droplet radius-squared. We expand upon a photochemical adaptation of the Finke–Watzky model to demonstrate that in all cases, volume-dependent photochemical reactions occur. Through systematic elimination of confounding factors, we establish that weak visible absorption in the low-energy tail of UV bands drives photochemistry across all of these organic solutes, demonstrating that extremely weak molar absorptivities can facilitate significant photochemical transformations in the confined environment of a microdroplet.

Received 18th September 2025,
Accepted 2nd December 2025

DOI: 10.1039/d5cp03615a

rsc.li/pccp

1 Introduction

Photochemistry is a fundamental driving force in both atmospheric chemistry and prebiotic chemical evolution.[1,2] In Earth's atmosphere, UV-driven formation of ozone and hydroxyl radicals shapes key oxidative pathways.[3,4] On early Earth, sunlight-enabled reactions likely contributed to the abiotic synthesis of essential biomolecular precursors.[2] Sutherland and co-workers demonstrated that UV irradiation can generate sugars, nucleotides, and lipid precursors from simple feedstocks under plausible prebiotic conditions.[5,6] In the field of prebiotic chemistry, aerosol microdroplets have long attracted attention as potential microreactors where such syntheses could proceed efficiently.[7–12] Vaida and collaborators first proposed that atmospheric aerosols could enable the accumulation of life's building blocks while mitigating the effects of bulk aqueous hydrolysis at the air–water interface.[7,10] Supporting this hypothesis, Nam *et al.* demonstrated the abiotic production of sugar phosphates and nucleosides within microdroplets,[13] and related droplet studies have achieved peptide formation from free amino acids.[11,14] However, recent work has shown that gas-phase processes are responsible for sugar phosphate yields in electrospray ionization microdroplet experiments, demonstrating the need to carefully examine reaction acceleration mechanisms.[15] Despite this progress, condensed-phase photochemistry, especially in microcompartmentalized environments such as aerosol droplets, remains less understood than its gas-phase counterpart. While it is known that droplets exhibit unique photochemical behavior distinct from that of bulk solutions, their mechanistic origins remain elusive.[16–18]

Aerosol microdroplets offer physical conditions that strongly enhance reaction rates and alter reaction pathways.[19–22] Their high surface-to-volume ratios facilitate efficient molecular interactions at air–water interfaces, while rapid evaporation allows solute concentrations to significantly exceed bulk solubility limits.[20,23] Such conditions can accelerate chemical transformations by several orders of magnitude compared to bulk solutions.[20,24] Moreover, aerosol droplets can act as microscopic optical cavities, intensifying the local electromagnetic field and amplifying incident light.[25–29] Signorell and co-workers have

[a] *Department of Chemistry, McGill University, Montreal, Quebec, Canada. E-mail: thomas.preston@mcgill.ca*
[b] *Department of Atmospheric and Oceanic Sciences, McGill University, Montreal, Quebec, Canada*

demonstrated, for example, that nanofocusing effects in droplets, markedly increasing photochemical reaction rates.[28,30] Despite substantial experimental results, fundamental questions remain about the mechanisms underlying droplet-accelerated photochemistry, especially for compounds with negligible visible-light absorption in dilute solutions.

Our recent studies demonstrated that visible irradiation of supersaturated droplets containing dicyandiamide promoted amide bond formation, a process strongly dependent on droplet size.[31] However, the precise mechanisms governing this behavior were unclear. Motivated by these findings, here we systematically investigate photochemistry in aqueous microdroplets containing biologically relevant, weakly absorbing organic solutes (glycine, proline, serine, glucose, ribose, and deoxyribose) at concentrations of 5 to 12 M under visible-light illumination (473 and 532 nm; peak focal intensity $I_0 \approx 32$ MW cm^{-2} in most experiments). We employ optical trapping combined with cavity-enhanced Raman spectroscopy to probe chemical transformations *in situ*. Remarkably, all of the investigated solutes undergo visible-light-driven reactions, exhibiting droplet-size-dependent kinetics indicative of autocatalytic processes. Through a systematic study of photochemical reactions in confined droplet environments, we demonstrate that weak visible light absorption in the low-energy tail of UV bands can drive significant photochemistry in organic solutes. By eliminating potential confounding factors including trace contaminants, laser-induced nucleation, multiphoton processes, dissolved oxygen effects, and dipole–dipole interactions, we establish that even extremely weak molar absorptivities ($\ll 10$ M^{-1} cm^{-1}) can facilitate observable photochemical transformations when combined with intense visible irradiation and high solute concentrations, revealing a mechanism for droplet photochemistry that is possible across a wide range of organic systems.

2 Results and discussion

2.1 Photochemical reactions in microdroplets

The photochemistry of aqueous microdroplets was studied using the setup depicted in Fig. 1a and described in the Materials and methods (Section 4.1). Single aqueous microdroplets are optically held using either a $\lambda = 473$ or 532 nm laser in a cell with a fixed relative humidity (RH). Raman scattering measurements provide both chemical information, *via* vibrational bands, and physical properties of the droplet through sharp morphology-dependent resonance (MDR) peaks (Fig. 1b and c). When MDR peaks are fitted using resonance positions

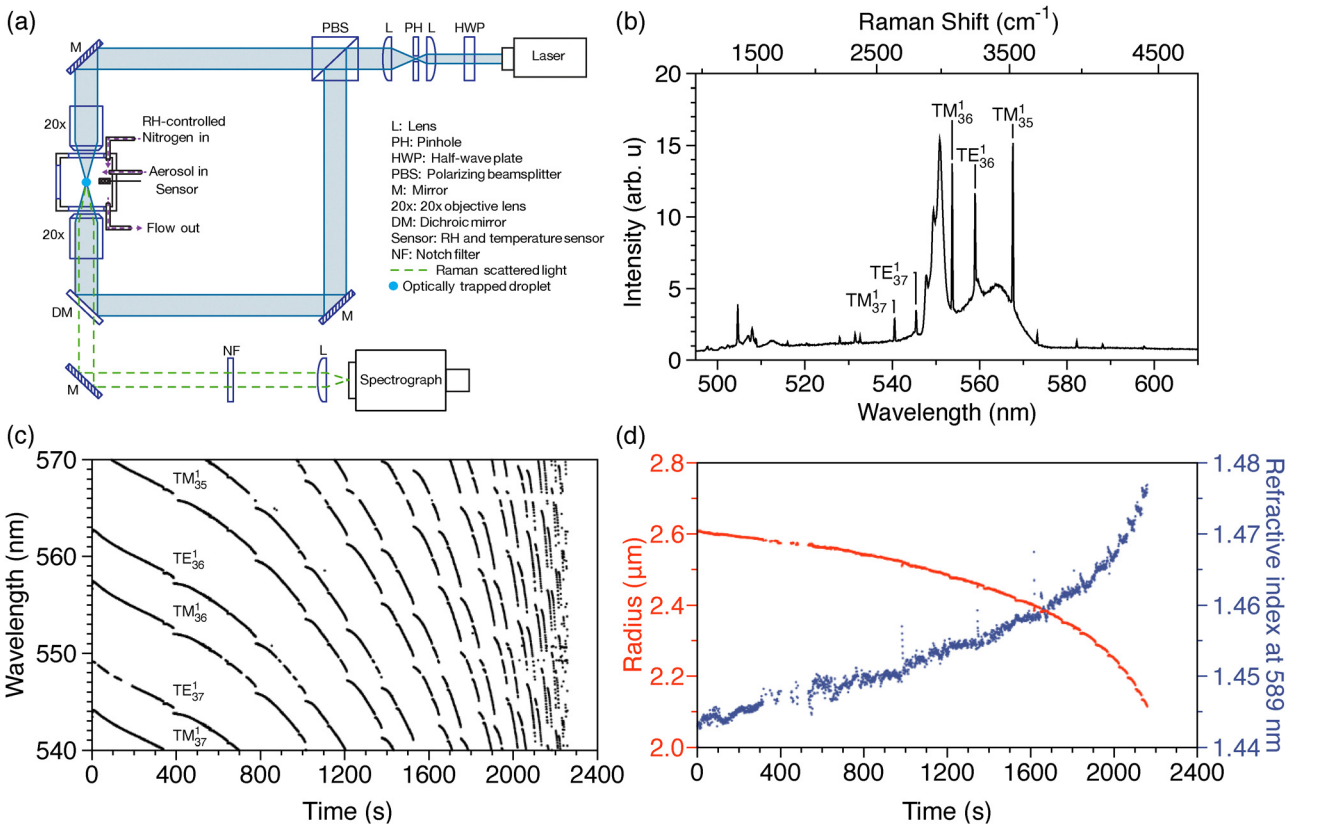

Fig. 1 (a) Schematic of the optical setup for suspending single aerosol droplets. (b) Representative Raman spectrum of an aqueous proline droplet. Transverse electric (TE) and transverse magnetic (TM) morphology-dependent resonances (MDRs) are labeled with mode orders and numbers identified using MRFIT.[32] (c) Temporal evolution of MDR peak positions for the droplet shown in (b) as its size decreases. (d) Droplet radius (red) and refractive index at 589 nm (blue) extracted over time from fitting the mode positions in (c) using MRFIT.

from Mie theory, droplet size and refractive index can be simultaneously retrieved with low uncertainty (±1 nm and ±0.0005, respectively).[32] Fig. 1d shows the fitted size and refractive index determined using the MDRs in Fig. 1c.

The type of physical behavior observed in Fig. 1d for aqueous proline is representative of all the aqueous organic systems studied in this work: for most of the measurement, the radius of the droplet decreases while its refractive index increases at a nearly linear rate. Near the end of the measurement, however, these changes deviate from the earlier linearity and begin to accelerate, leading to the droplet becoming unstable and eventually falling out of the optical trap.

Prior to a more detailed analysis, we first emphasize that the observed changes in Fig. 1d cannot be solely attributed to evaporation. In an aqueous droplet containing a single solute in equilibrium with the gas phase at a fixed RH, if the solute evaporates, water must also evaporate to maintain equilibrium with the surrounding RH. This scenario would lead to a constant refractive index over time, as the solute concentration remains unchanged. For instance, Fig. S1 and S2 show typical examples of radius and refractive index measurements obtained from MDR analysis of optically trapped droplets in a fixed-RH environment, involving aqueous droplets containing non-volatile (LiCl) and volatile (1,2,6-hexanetriol) solutes, respectively, where no chemical reaction occurs. In these two examples, the refractive index remains constant throughout the measurements. However, in the case of Fig. S2, the hexanetriol evaporates so the droplet size decreases over time. Neither behavior is observed for the aqueous organic droplet in Fig. 1d, indicating that additional processes, such as chemical reactions or phase transitions, must be contributing to the changing refractive index and size. Here, we argue that, in fact, both processes are occurring: a photochemical reaction yields a product with a hygroscopicity that is significantly lower than that of the reactant, leading to water loss. Product formation eventually leads to a phase transition (precipitation), causing the droplet to fall out of the trap. Water loss can also be confirmed by examining the decrease in intensity of the OH stretching band of water during the measurement (Fig. S3 and S4).

In Section 4.2, we present a model to determine solute concentration from refractive index measurements. This model is based on the assumption that the aqueous droplet is always in equilibrium with its surrounding RH and contains two solutes: the reactant and the product. The hygroscopicity of both solutes is determined using κ-Köhler theory. Refractive index is used to determine concentration here rather than Raman intensity because (i) the supersaturation of all droplets makes it difficult to obtain an accurate calibration curve, and (ii) Mie scattering affects Raman intensity, complicating quantitative analysis. Examples of (ii) are shown in Fig. S5.

Fig. 2 and 3 show the time-dependent radii and reactant concentrations for aqueous solutions of amino acids and sugars, respectively. Each measurement was performed at several different initial droplet radii. In all cases, we observe an initial induction period with only small changes in reactant concentration or droplet size, followed by a shorter period of reaction acceleration in which both concentration and droplet size decrease sharply. During this second period, the droplets become unstable and eventually fall out of the optical trap. At this time, the measurements end.

The kinetics observed here, which consist of an induction period followed by rapid reaction acceleration, are characteristic of autocatalysis (*i.e.*, prior to droplet loss, the concentration measurements show sigmoidal or S-shaped curve behavior). In Section 2.2 we explore such a model and its predictions regarding the effects of varying droplet size, laser power, and reactant concentration. Prior to that, we first consider an alternative explanation: the low hygroscopicity of the photoproduct leads to water loss from the droplets, resulting in an increased reactant concentration as the droplet size decreases. As more photoproduct forms, additional water is lost, causing the droplet size to decrease more rapidly and further concentrating the reactant. This process, in turn, accelerates the rate of photoproduct formation. This hypothesis is not plausible and can be rejected. First, as the reactant is consumed during droplet size reduction, the extent to which its concentration can increase is limited. Second, thermodynamic calculations show that the initial reactant concentrations (5 to 12 M) are all supersaturated, which limits any further increase in concentration during the reaction. Therefore, while the concentrating effect due to droplet size reduction may contribute to a slight increase in the reaction rate, it is not the primary mechanism driving the kinetics. To better explain the observed behavior, we explore a model that incorporates autocatalysis.

2.2 Photochemical reaction mechanism and kinetic modeling

We model the kinetics the observed photochemical reactions with the following set of chemical equations

$$\mathrm{A} + h\nu \xrightarrow{\sigma_\mathrm{A} I} \mathrm{A}^*, \tag{1a}$$

$$\mathrm{A}^* \xrightarrow{k_{\mathrm{ex1}}} \mathrm{A}, \tag{1b}$$

$$\mathrm{A}^* \xrightarrow{k_1} \mathrm{B}, \tag{1c}$$

$$\mathrm{A}^* + \mathrm{B} \xrightarrow{k_{\mathrm{ex2}}} \mathrm{A} + \mathrm{B}, \tag{1d}$$

$$\mathrm{A}^* + \mathrm{B} \xrightarrow{k_2} \mathrm{B} + \mathrm{B}, \tag{1e}$$

where A is the reactant, A* is its excited state, B is the photoproduct, σ_A is the molecular absorption cross-section of species A, and I is the intensity of light (in photons per area per time). The rate constants are defined as follows: k_{ex1} is for the deactivation of A*, k_1 is for the transformation of A* to B, k_{ex2} is the deactivation of A* by B to its ground state, and k_2 is for the reaction between A* and B to further produce B.

The reaction mechanism described above can be viewed as a photochemical adaptation of the Finke–Watzky model,[33] which is widely used to describe autocatalytic processes in chemical kinetics.[34,35] Autocatalysis is evident in reaction (1e), where the product B accelerates its own formation by interacting with the

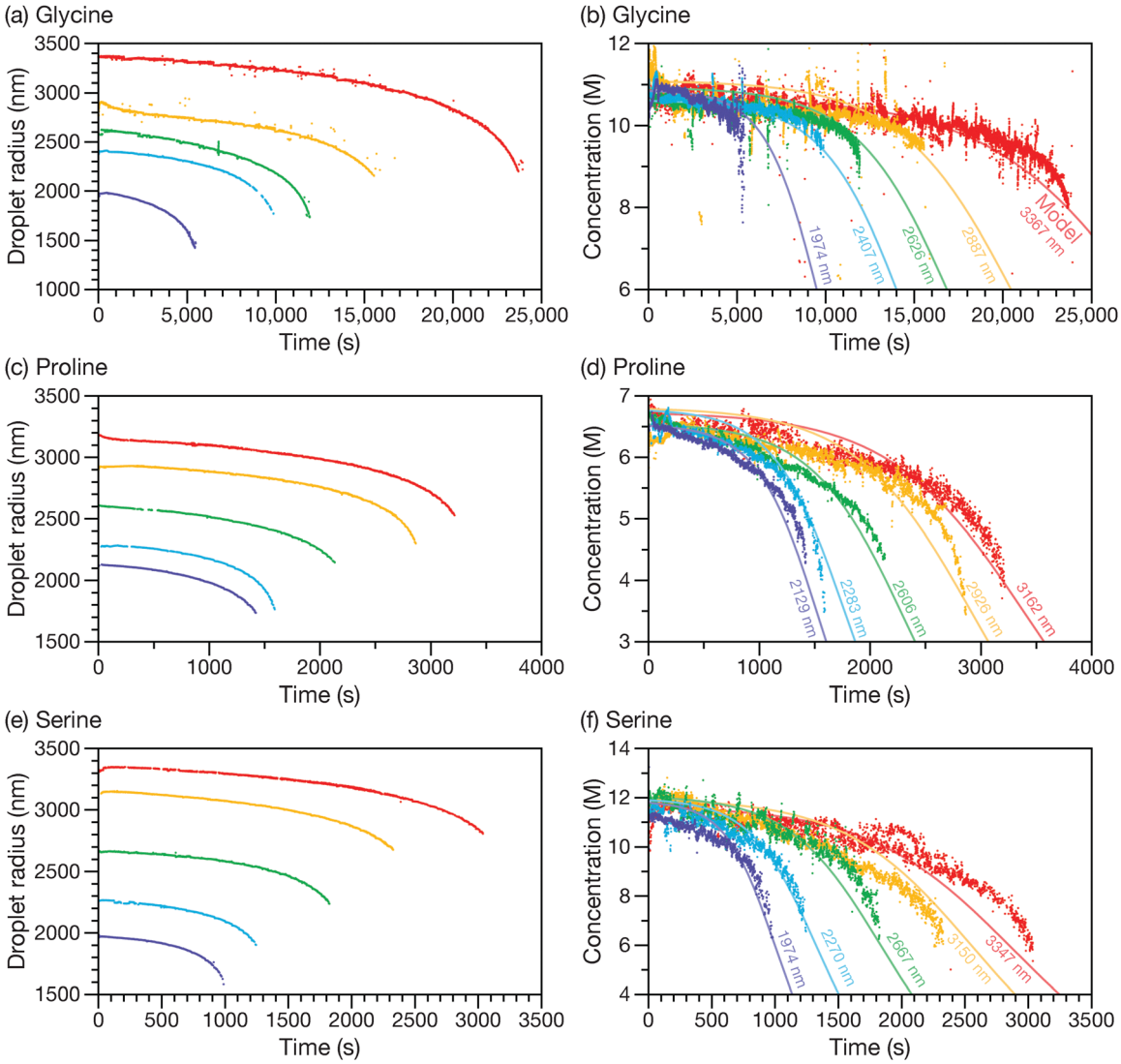

Fig. 2 Droplet radius (left column) and solute concentration (right column) as a function of time for aqueous solutions of glycine, proline, and serine at different initial droplet radii. At t = 0, all droplets are a binary solution of water and the listed solute. Panels (a) and (b) show data for glycine, panels (c) and (d) for proline, and panels (e) and (f) for serine. Concentrations were determined using refractive index measurements and methodology described in Section 4.2. Data points correspond to experimental measurements and the solid lines represent model fits using eqn (2) with the parameters in eqn (3). The two parameters of best-fit for each solute, ϕ_2/ϕ_1 and $\sigma_A\phi_2$, are listed in Table S2. The initial radii used in the model calculations are indicated next to each corresponding line. The RH during the experiments was 68 ± 1% for glycine, 66 ± 1% for proline, and 63 ± 1% for serine. All measurements were performed using a λ = 473 nm laser at 500 mW.

excited reactant A*. The steps outlined are pseudo-elementary steps, meaning they are simplified representations of more complex underlying processes.[35] This simplification allows for effective kinetic modeling by focusing on the key transformations and interactions without detailing every elementary reaction. While some mechanistic details are condensed or omitted, this approach enables us to define effective quantum yields and capture the essential kinetics governing the photochemical system.

In Section 4.3, we demonstrate how the integrated rate law for reactions (1a)–(1e) can be approximated by the sigmoidal function

$$c_A(t) = c_{A_0}\frac{1}{1+\exp[\beta(t-t_0)]}, \quad (2)$$

where c_{A_0} is the initial concentration of A at $t = 0$, t_0 is the time at which the rate of concentration change reaches its maximum (for either the loss of A or formation of B), and β is the curve steepness parameter. A larger β indicates a more rapid concentration change near t_0.

Expressions for t_0 and β are derived in Section 4.3 for both surface- and volume-based photochemistry in a droplet of radius r, illuminated by a Gaussian beam under the condition that the droplet radius is larger than the beam waist. In our analysis here, we will set r to the initial droplet radius, r_0. For photochemistry occurring throughout the entire droplet volume, the parameters in eqn (2) are given by

$$t_0 = \frac{\pi r_0^2}{\sigma_A \Phi}\frac{\ln(\phi_2 c_{A_0}/\phi_1)}{\phi_1+\phi_2 c_{A_0}} \quad \text{and} \quad \beta = \frac{\sigma_A \Phi}{\pi r_0^2}(\phi_1+\phi_2 c_{A_0}), \quad (3)$$

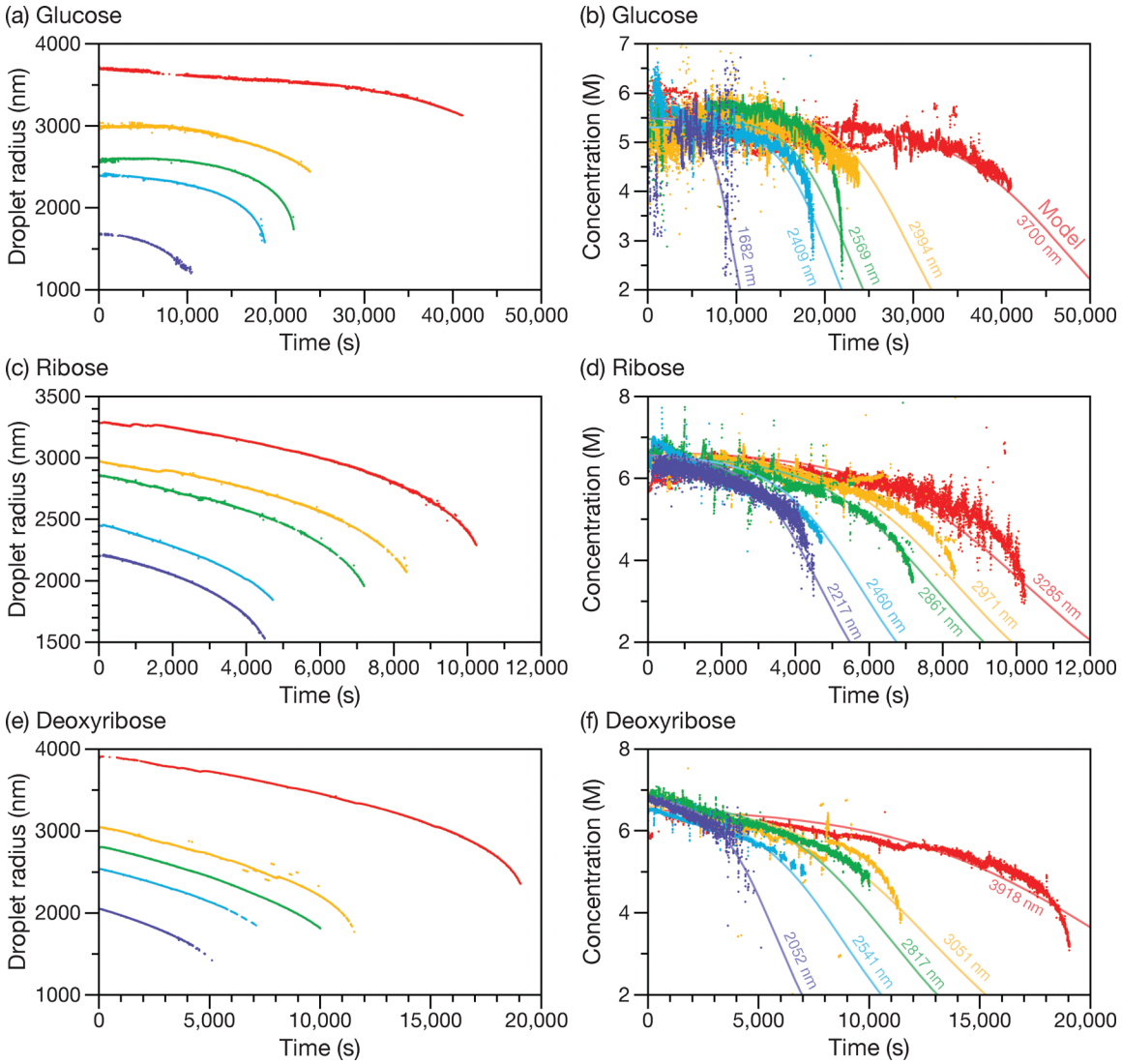

Fig. 3 Droplet radius (left column) and solute concentration (right column) as a function of time for aqueous solutions of glucose, ribose, and deoxyribose at different initial droplet radii. At t = 0, all droplets are a binary solution of water and the listed solute. Panels (a) and (b) show data for glucose, panels (c) and (d) for ribose, and panels (e) and (f) for deoxyribose. Concentrations were determined using refractive index measurements and methodology described in Section 4.2. Data points correspond to experimental measurements and the solid lines represent model fits using eqn (2) with the parameters in eqn (3). The two parameters of best-fit for each solute, ϕ_2/ϕ_1 and $\sigma_A\phi_2$, are listed in Table S2. The initial radii used in the model calculations are indicated next to each corresponding line. The RH during the experiments was 72 ± 2% for glucose, 67 ± 1% for ribose, and 66 ± 1% for deoxyribose. All measurements were performed using a λ = 473 nm laser at 500 mW.

where Φ is the photon rate of the beam, and ϕ_1 and ϕ_2 are the effective quantum yields for the photochemical pathways in reactions (1a) and (1e), respectively (see Section 4.3 for more details).

For photochemistry occurring only at the droplet surface (thickness δ), the parameters in eqn (2) are given by

$$t_0 = \frac{\pi r_0^3}{3\delta\sigma_A\Phi}\frac{\ln\left(\phi_2 c_{A_0}/\phi_1\right)}{\phi_1 + \phi_2 c_{A_0}} \quad \text{and}$$
$$\beta = \frac{3\delta\sigma_A\Phi}{\pi r_0^3}\left(\phi_1 + \phi_2 c_{A_0}\right). \tag{4}$$

As t_0 is the inflection point of the sigmoidal curves that depict the concentration of A over time, it is well constrained by measurements and easy to identify experimentally. Size-dependent measurements of t_0 provide an accurate way to determine whether surface or volume-dependent photochemistry is taking place for a droplet in a Gaussian beam. From eqn (3) and (4), we see that t_0 will be proportional to the radius-squared during volume-dependent photochemistry and proportional to the radius-cubed during surface-dependent photochemistry. These relationships are counterintuitive, but can be applied here. Fig. 4 shows measurements of t_0 as a function of the r_0 along with best-fit curves proportional to either the square (r_0^2) or the cube (r_0^3) of the initial radius, as well as a fit where the exponent n is allowed to vary (r_0^n). For the aqueous amino acids, panels (a–c), the best-fit exponent consistently falls between the squared and cubed fits, suggesting

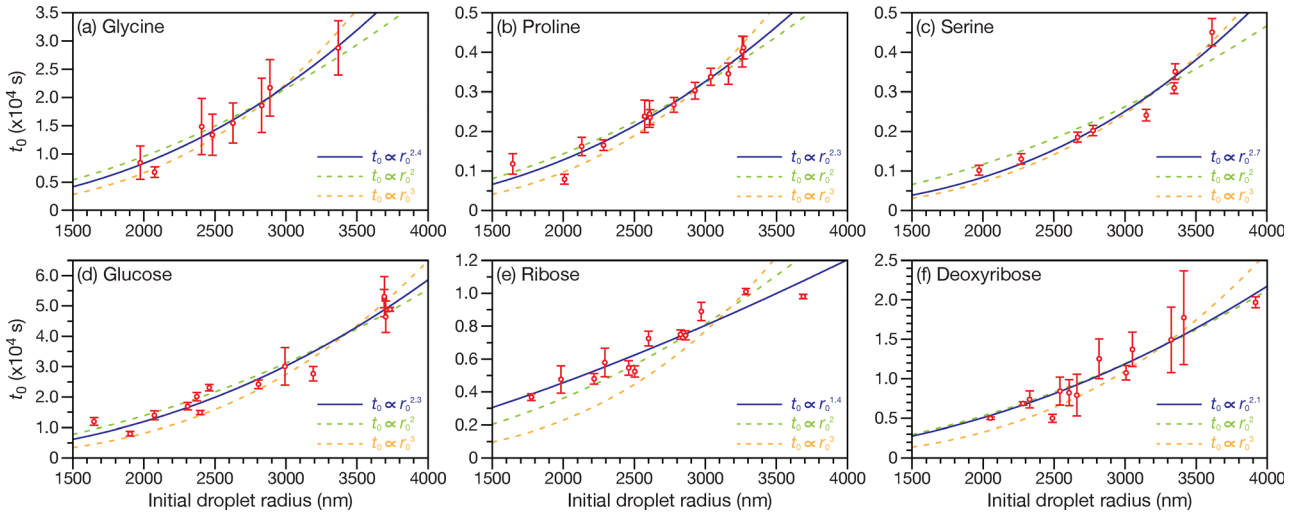

Fig. 4 Inflection point (t_0) determined from the sigmoidal fits to concentration for individual droplets as a function of initial droplet radius (r_0). Panels (a)–(c) show measurements for the amino acids: glycine, proline, and serine respectively. Panels (d)–(f) show measurements for saccharides: glucose, ribose, and deoxyribose. Error bars were calculated by propagating the uncertainties in the fitted parameter t_0 (obtained with eqn (2)) together with the uncertainty in the initial droplet-coalescence time. Best-fit curves for measurements using functions proportional to powers of the initial radius, r_0^n, are shown. During the fits, the exponent n is either fixed at $n = 2$ or $n = 3$ (dashed lines) or allowed to vary (solid line). The RH during the experiments was (a) 67 ± 1%, (b) 66 ± 1%, (c) 63 ± 1%, (d) 71 ± 1%, (e) 66 ± 1%, and (f) 66 ± 1%, which corresponds to initial solute concentrations of (a) 11.1 ± 0.3 M, (b) 6.7 ± 0.1 M, (c) 11.9 ± 0.1 M, (d) 5.6 ± 0.1 M, (e) 6.8 ± 0.1 M, and (f) 6.8 ± 0.2 M. All measurements were performed using a λ = 473 nm laser at 500 mW.

either a mixed dependence on volume and surface effects or that our application of the Finke–Watzky model is too simplified to capture what are more complex kinetics. In contrast, for the aqueous sugars, panels (d–f), the best-fit exponent remains close to the squared fit, indicating a predominantly volume-dependent process. Therefore, we conclude that there is no evidence that the observed chemical transformations occur solely at the droplet surface. Instead, they likely occur predominantly throughout the droplet volume, as shown in panels (e–f), or at least partially, as shown in panels (a–c).

The validity of the proposed kinetic model can be further evaluated by trapping droplets of similar sizes while systematically varying either the initial concentration of species A (Fig. 5) or the laser power (Fig. 6). Fig. 5 illustrates the

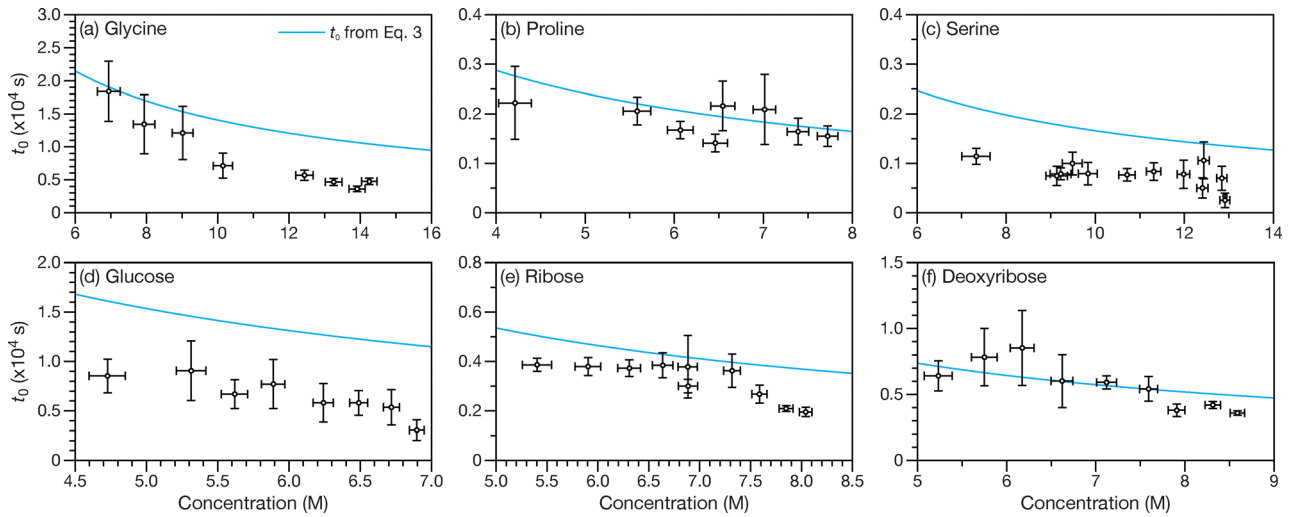

Fig. 5 Inflection point (t_0) determined from the sigmoidal fits to time-dependent solute concentration for individual droplets as a function of initial solute concentration. Panels (a)–(c) show measurements for the amino acids: glycine, proline, and serine respectively. Panels (d)–(f) show measurements for saccharides: glucose, ribose, and deoxyribose. RH in the trapping cell was varied between measurements as this determines the initial solute concentration. Vertical error bars (t_0) were calculated as described in the caption of Fig. 4, while horizontal error bars (concentration) were determined from the uncertainty in the cell RH. The model predictions for t_0 (solid lines) were calculated using the expression in eqn (3) and the fitted parameters from Fig. 2 and 3 (listed in Table S2). All measurements were performed using a λ = 473 nm laser at 500 mW. To minimize size effects, droplets of similar radii were trapped for the set of measurements shown in each panel. The initial droplet radii were (a) 2284 ± 132 nm, (b) 2355 ± 217 nm, (c) 2370 ± 375 nm, (d) 2031 ± 148 nm, (e) 2117 ± 80 nm, and (f) 2078 ± 96 nm.

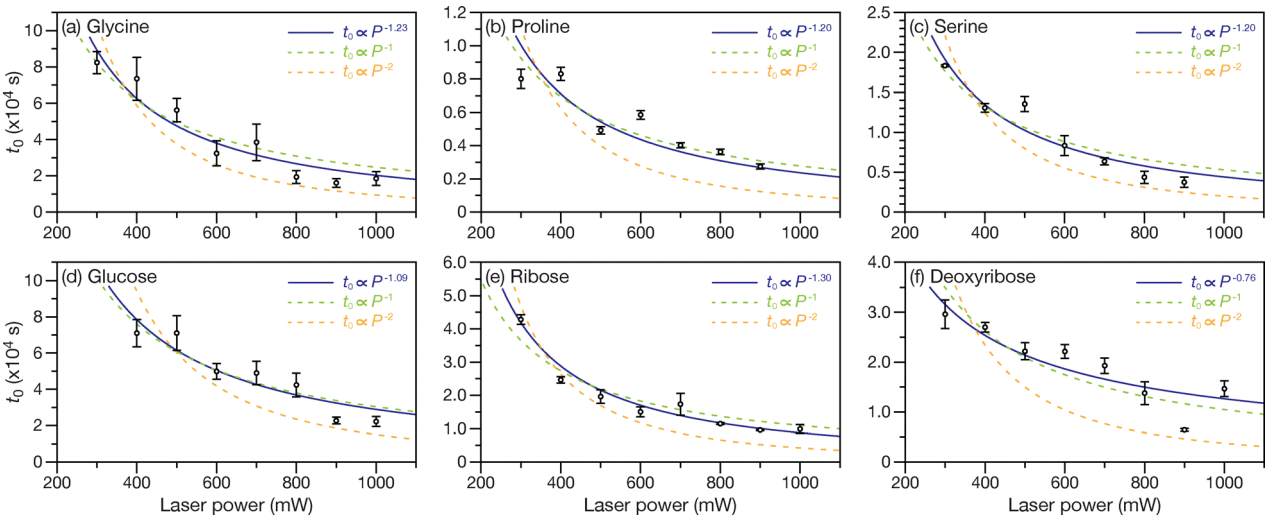

Fig. 6 Inflection point (t_0) determined from the sigmoidal fits to time-dependent solute concentration for individual droplets as a function of laser power, P, using a λ = 532 nm laser. Panels (a)–(c) show measurements for the amino acids: glycine, proline, and serine respectively. Panels (d)–(f) show measurements for saccharides: glucose, ribose, and deoxyribose. Measurements were fitted as a function of laser power using the expression for t_0 from eqn (3) (solid lines). Error bars were calculated using the method described in the caption of Fig. 4. Best-fit curves for measurements using functions proportional to powers of the laser power, P^n, are shown. During the fits, the exponent n is either fixed at $n = -1$ or $n = -2$ (dashed lines) or allowed to vary (solid line). The RH during the experiments was (a) 63 ± 1%, (b) 65 ± 1%, (c) 65 ± 1%, (d) 64 ± 1%, (e) 63 ± 1%, and (f) 63 ± 1%, which corresponds to initial solute concentrations of (a) 12.1 ± 0.2 M, (b) 6.8 ± 0.1 M, (c) 11.6 ± 0.2 M, (d) 6.2 ± 0.1 M, (e) 7.1 ± 0.1 M, and (f) 7.1 ± 0.1 M. To minimize size effects, droplets of similar radii were trapped for the set of measurements shown in each panel. The initial droplet radii were (a) 2538 ± 51 nm, (b) 3122 ± 118 nm, (c) 2496 ± 168 nm, (d) 2456 ± 115 nm, (e) 2782 ± 203 nm, and (f) 2754 ± 100 nm.

dependence of t_0 on the initial solute concentration, which is controlled by adjusting the RH in the trapping cell. The relationship between RH and solute concentration is described in Section 4.2. From these concentration measurements, it can be seen that the experimentally measured dependence of t_0 is in agreement with the model predictions. However, the sensitivity is fairly weak across the accessible concentration range.

Fig. 6 shows the dependence of t_0 on laser power at a wavelength of 532 nm. Although all other measurements in this study were performed using a 473 nm laser, using a 532 nm laser here demonstrates that the observed photochemistry occurs across a broader region of the visible spectrum. From a practical perspective, the 532 nm laser in our lab can achieve significantly higher power levels compared to the 473 nm laser, which cannot go above 500 mW and requires at least 300 mW to reliably trap droplets. Thus, the 532 nm laser is better suited for systematically investigating the laser power dependence of t_0. The measurements show good agreement with the model prediction in either eqn (3) or eqn (4), confirming that t_0 is inversely proportional to laser power. The laser power-dependent measurements are also important because they rule out the possibility of a two-photon process, which, although unlikely under our experimental conditions, would yield an inverse-square dependence of t_0 on laser power.[36]

The concentration measurements shown in panels (b, d and f) of Fig. 2 and 3 were also fitted with the integrated rate law (eqn (2)). In all cases, the volume-dependent photochemistry parameters from eqn (3) were used. For each binary aqueous system fitted with this model, there are only two free parameters when fitting across multiple sets of concentration data. These fitting parameters are the ratio ϕ_2/ϕ_1 and the product $\sigma_A\phi_2$. The best-fits are listed in Table S2. In both Fig. 2 and 3, the experimental size-dependent concentration-time profiles are reasonably well-described by the best-fit to the integrated rate law, supporting the validity of the autocatalysis model.

The most common discrepancy when fitting measurements is that the model does not always capture the steep acceleration seen as t_0 is approached. Incorporating the effects of shrinking droplet size into the rate-law derivation could lead to more accurate predictions of the observed steep accelerations near t_0 and better overall agreement with experimental results, although this is likely a small correction. More significantly, including subsequent steps in the mechanism would enhance the predicted self-acceleration (and steepness). For example, further autocatalytic reactions involving the photoproduct B and its excited state could enhance the predicted self-acceleration. Fig. S4 shows the measured Raman spectra for aqueous glucose, ribose, and deoxyribose as the photochemical reaction proceeds. All of these solutes show the appearance of a band near 1700 cm^{-1}, indicating formation of carbonyl-containing products. Under the nitrogen atmosphere used in all experiments, direct oxidation of hydroxyl groups by molecular oxygen is unlikely. Instead, the most probable mechanism involves photochemical cleavage of the C1–O5 bond, leading to ring opening and formation of aldehyde fragments, consistent with prior UV photolysis studies of glucose.[37,38] The carbonyl-containing photoproducts absorb in the near-UV region,[39] and their absorption cross section at the trapping wavelengths is expected to be much larger than that of the corresponding species A. Therefore, even small amounts of such products could contribute to the autocatalytic kinetics.

2.3 Weak optical absorption of aqueous organics in microdroplets

The model presented in Section 2.2 largely accounts for the observed size-dependent kinetics, but it does not explain why certain organic molecules, often described as "non-absorbing" in dilute aqueous solutions, become photoexcitable by visible light in droplets. Since this phenomenon appears in many different aqueous organic systems, the underlying physical mechanism must be broadly applicable, rather than chemically specific. All of these molecules exhibit strong UV absorption bands, as shown in Fig. S7 (the Lorentzian parameters for their lowest-energy UV bands, used in calculations here, are listed in Table S3). Another feature that all of these systems have in common is their high concentration, as shown in panels (b, d and f) of Fig. 2 and 3, where initial solute concentrations range from 5 to 12 M (all supersaturated). In these high concentration aqueous solutions, the average intermolecular spacing between solutes fluctuates around molecular dimensions. One hypothesis would be that, under these conditions, solute molecules become sufficiently close for intermolecular dipole–dipole interactions to become significant. Dipole–dipole interactions are known to significantly shift or broaden molecular absorption features. These excitonic coupling effects often lead to substantial hypsochromic (blue) or bathochromic (red) shifts in absorption spectra, as demonstrated extensively with H- and J-aggregates (*e.g.*, in concentrated solutions of organic dyes).[40–42] As a result, molecules that exhibit negligible visible absorption in dilute solutions can become strongly absorbing at visible wavelengths due to excitonic coupling at high concentrations. Here, the coupling would shift far UV bands, or at least further shift their tails, into the visible.

We explored the above hypothesis using both a coupled-dipole model and an effective-medium model.[43] The effective-medium model treats the solute and solvent molecules as a homogeneous continuum whose dielectric function is obtained from the single-molecule polarizability through the Clausius–Mossotti relation (see SI). This approximation is particularly useful for spherical particles larger than several nanometers, as explicit coupled-dipole calculations with more than approximately 10^4 dipoles become computationally prohibitive due to memory constraints. All computational details and parameters are provided in the SI. Fig. S9–S12 in the SI provide the full set of calculations, while Fig. 7 shown here presents representative results for a single system (aqueous proline).

We first examined dipole pairs arranged in a head-to-tail orientation, which typically leads to the largest red shifts in absorption.[40,42,43] This configuration provides an upper bound on what to anticipate in terms of increased absorption. Fig. 7a and more extensive calculations in Fig. S9 show that decreasing the dipole-to-dipole distance to 0.5 nm increases the molecular absorption cross-section at visible wavelengths by only a small amount. Next, we applied the model to a more realistic dipole

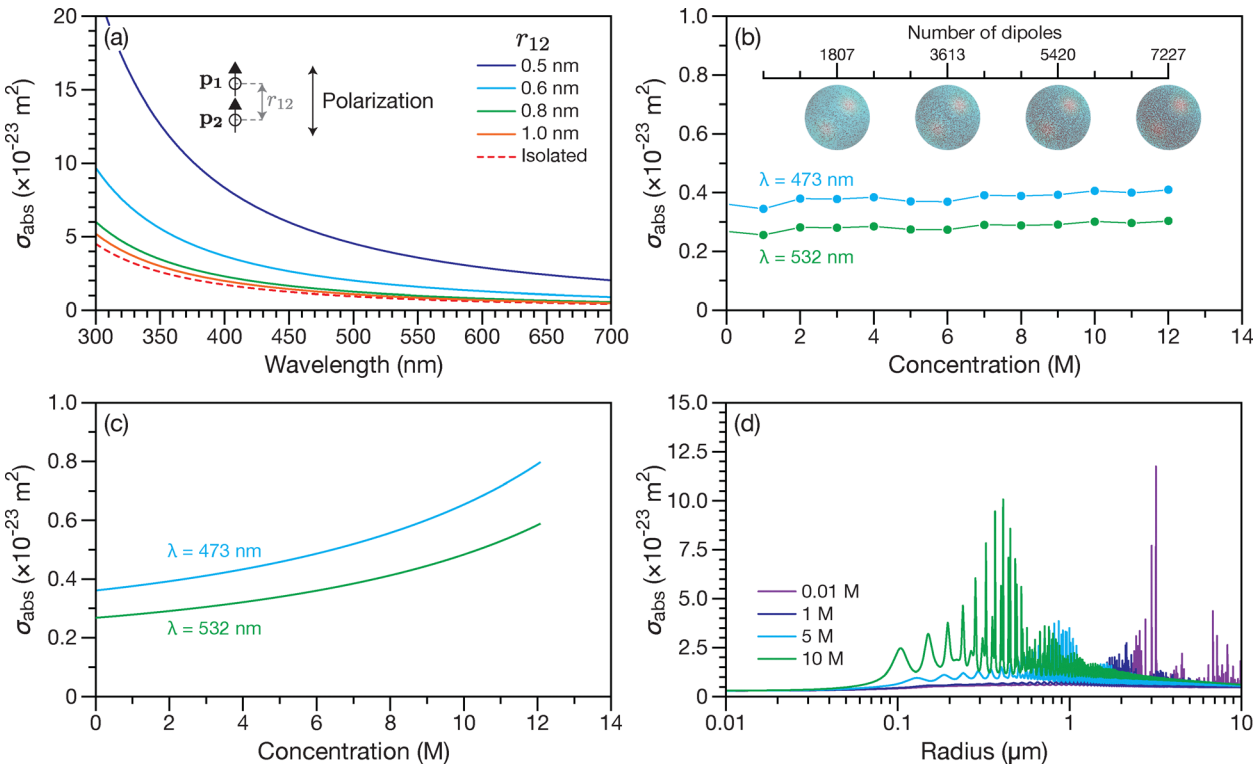

Fig. 7 Absorption cross-section per dipole, σ_{abs}, for proline. Coupled-dipole model: (a) two dipoles separated by a center-to-center distance r_{12}, and (b) randomly oriented and positioned dipoles contained within a 10 nm radius sphere with the number of dipoles set by the bulk concentration. Effective-medium model: (c) σ_{abs} as a function of aqueous proline concentration, and (d) σ_{abs} for a homogeneous 10 nm radius sphere calculated with full Mie theory at λ = 473 nm. See the SI for computational details and more extensive results.

arrangement by randomly positioning and orienting the dipoles within a spherical volume. This produced only very small increases in the molecular absorption cross-section at the two optical wavelengths used in our experiments, even when coupling between thousands of closely spaced dipoles (Fig. 7b and Fig. S10). The effective-medium model likewise predicts a small increase in the molecular absorption cross-section at these visible wavelengths for both bulk systems (Fig. 7c and Fig. S11) and microdroplets (Fig. 7d and Fig. S12). Overall, dipole–dipole coupling increases visible-light absorption only slightly relative to that of isolated molecules.

Then why do photochemical transformations occur in these systems? In this work, we have established that the photochemistry is similar across many solutes and occurs throughout the droplet volume. Further, we have shown that it cannot be explained by (i) multiphoton absorption, (ii) dipole–dipole coupling, (iii) the presence of dissolved molecular oxygen, (iv) trace contaminants, or (v) laser-induced nucleation (see Section 4.1.4). We therefore propose that it is initiated by absorption in the low-energy tail of the strong UV bands of the organic solutes. As illustrated for glycine in Fig. 8a, the visible-band absorptivity is orders of magnitude below the UV band maximum (results for all solutes are shown in Fig. S7). Calculated visible cross-sections from the Lorentz best-fit are on the order of 10^{-24} m^2 molecule^{-1} (Fig. 7b–d), corresponding to molar absorptivities of less than 10 M^{-1} cm^{-1}. However, the true absorption cross-section will be far smaller than these already small estimates, as the Lorentz-oscillator model used here is known to overpredict absorption in the low-energy tails.[44] The Voigt model, which is known to provide a more accurate description of the low-energy tails,[44] yields visible band cross-sections that are lower, but still on the same order of magnitude. In spite of this extremely weak absorptivity, the combination of intense visible irradiation and high solute concentrations in a confined environment is still sufficient to drive the photochemical reactions forward on timescales of minutes.

This interpretation is consistent with our previous work on dicyandiamide (DCD).[31] In a λ = 532 nm optical trap, DCD undergoes photochemical transformation far more quickly than any system investigated here, with reaction times roughly ten times shorter than the fastest amino-acid or sugar droplets. With the λ = 473 nm trap used in most of the present experiments, t_0 for DCD was typically <100 s for droplets of comparable size. Fig. S8 shows that the lowest-energy UV absorption band of DCD is both closer to the visible region and more intense than those of the other solutes. The long-wavelength tail of this band leads to a higher absorption cross section at visible wavelengths compared to the other solutes, which in turn explains its comparatively rapid photochemistry.

We have also previously shown that aqueous droplets containing inorganic solutes (*e.g.*, NaCl, $(NH_4)_2SO_4$) absorb visible light (λ = 532 nm) despite typically being regarded as non-absorbing at optical wavelengths. This absorption arises from the long-wavelength tails of electronic UV transitions.[46,47] In these systems, no chemical transformation occurs, and the absorption only leads to heating, which causes the droplet to shrink when laser power is increased. This size change is monitored *via* MDRs, allowing the imaginary part of the refractive index to be measured directly. For those inorganic solutes, the imaginary refractive indices range from 10^{-8} to 10^{-7} (corresponding to absorption cross-sections on the order of 10^{-29} to 10^{-28} m^2 molecule^{-1}). The order of magnitude of these absorption cross-sections is likely representative of the true values for the organic solutes studied here.

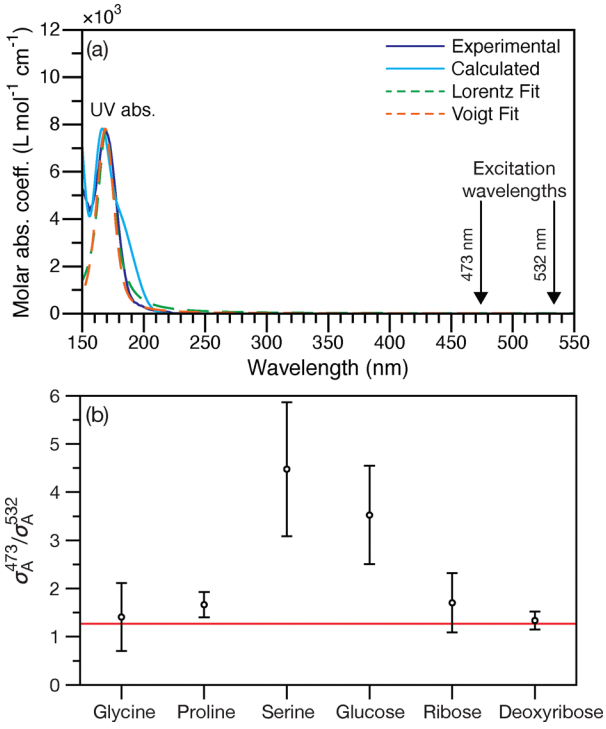

Fig. 8 (a) Measured (dark blue) and calculated (light blue) molar absorptivity spectra for aqueous glycine. The measured spectrum is from ref. 45. The calculated curves are time-dependent DFT (TD-DFT) results (see the SI for details). The dashed green line is a single Lorentzian fit to the measured spectrum, with parameters listed in Table S3. The dashed orange line is a fit to the measured spectrum using the Voigt model, with parameters listed in Table S3 and a fraction, *f*, of 0.5. (b) Measured ratio of the molecular absorption cross-section at λ = 473 nm to that at λ = 532 nm, $\sigma_A^{473}/\sigma_A^{532}$. The solid red line shows the value expected if absorption at 473 nm and 532 nm arises solely from the long-wavelength tail of a UV electronic transition.

The absorption cross-sections for these systems could not be measured directly because it involves tracking droplet size while gradually varying the beam power. This experiment would have been confounded by simultaneous size changes from the chemical reaction. However, the product $\sigma_A\phi_2$ is one of the fitting parameters in the photochemical mechanism. If we assume that ϕ_2 is the same at both λ = 473 nm and λ = 532 nm, then the ratio of the absorption cross-sections, $\sigma_A^{473}/\sigma_A^{532}$, can be determined from the measurements. Because both 532 nm and 473 nm lie well to the red of the electronic resonance wavelengths (<200 nm) for these solutes, we can apply a long-wavelength single-molecule expression to predict the absorption ratio. In the Lorentzian model, this gives $\sigma_A^{473}/\sigma_A^{532} \approx (532/473)^2 = 1.265$ (see eqn (S20) and its derivation in the SI).

Fig. 8b compares the experimental ratio for the six solutes studied with this expected value (red line). Glycine, proline,

ribose, and deoxyribose agree well with this prediction given their experimental uncertainties. In contrast, serine and glucose measurements give larger ratios. Serine was the fastest reacting of all the systems, so it is possible that its absorption tail is not accurately captured by a single Lorentzian oscillator and/or that the long-wavelength approximation is no longer valid. For glucose, the higher ratio is probably due to its comparatively noisy data, which made accurate fitting of β difficult. Taken together, our results indicate that weak absorption in the visible wavelength tails of UV bands provides a likely explanation for the observed photochemistry in these concentrated microdroplets.

3 Conclusions

Our work reveals that visible-light photochemistry in aqueous microdroplets is possible for a wide range of organic solutes. The reactions occur throughout the droplet volume and are initiated by absorption in the low-energy tail of organic solutes. Experiments confirm that the chemistry cannot be ascribed to trace contaminants, laser-induced nucleation, multiphoton excitation, or dissolved O_2. Instead, confinement, intense visible light, and molar-level concentrations within the droplet combine to overcome very weak absorption cross sections, enabling photochemical transformation of nominally non-absorbing organics. Kinetic analysis shows that the photochemistry follows a Finke–Watzky two-step autocatalytic mechanism: a slow induction period is followed by rapid autocatalytic propagation, with the inflection time t_0 scaling as r_0^2/Φ for droplets irradiated in a Gaussian beam. By themselves, these reactions are unlikely to be directly useful, as they do not generate biologically important molecules (*e.g.*, no amide or glycosidic bonds are formed under the conditions studied here). However, the synthetic potential of this type of photochemistry was demonstrated in earlier work, where DCD was shown to drive amide bond formation in the presence of glycine.[31] Overall, the physical insights provided here establish a framework for exploring and applying more complex confined, low-absorptivity photochemistry in microdroplets.

4 Materials and methods

4.1 Single microdroplet measurements

4.1.1 Materials. Glycine (>99%, Thermo Scientific), serine (>99%, Sigma-Aldrich), proline (99%, Sigma-Aldrich), D-glucose (>99%, Sigma-Aldrich), D-ribose (99%, Fisher Scientific), 2-deoxy-D-ribose (99%, Fisher Scientific), lithium chloride (>99%, MP Biomedicals), 1,2,6-hexanetriol (96%, Sigma-Aldrich), and dicyandiamide (99%, Sigma-Aldrich) were purchased commercially and used without further purification. Aqueous solutions were prepared in deionized water to concentrations of approximately 0.5 M or to saturation. Higher concentration solutions allowed for larger droplets to be trapped.

4.1.2 Optical trap setup and experimental conditions. Single aerosol droplets were suspended in a dual-beam optical trap (Fig. 1a), the configuration of which has been described in detail elsewhere.[46,48] Briefly, the light from a continuous-wave laser was divided into two arms with a polarizing beam splitter (PBS251, Thorlabs) and each arm was focused with a long working distance objective (Plan APO ELWD 20X/0.420 WD = 20 mm, Motic). The effective beam waist at the focal point was approximately 1 μm.[49] The optical trap was modified for investigating photochemical transformations using two trapping and excitation wavelengths: λ = 473 nm (Gem 473, Laser Quantum) and λ = 532 nm (Opus 532, Laser Quantum). For experiments utilizing the λ = 473 nm laser, the power was maintained at 500 mW to ensure stable trapping. The optical trap alignment was kept consistent across all experiments for a given system to standardize the light intensity experienced by individual droplets.

Aerosol droplets were generated and introduced into the trapping cell by nebulizing the bulk aqueous solutions with a medical nebulizer (TurboBOY SX, PARI). Within the cell, individual aerosol droplets were suspended near the overlapping focal points of the two laser beams. Suspended droplets were allowed to grow by coalescence to the desired radius. The RH in the cell was controlled by adjusting the ratio of a humidified and a dry nitrogen flow (UHP grade), regulated by mass flow controllers (MF-1, MKS Instruments). A total gas flow of 100 sccm was maintained throughout the experiments. For comparative studies, experiments were also performed under an air atmosphere, achieved by substituting the nitrogen carrier gas with UHP air. The temperature and RH inside the cell were monitored using a sensor (SHT85, Sensirion) positioned near the trapped droplet (within 10 mm). All experiments were conducted at room temperature.

4.1.3 Raman spectroscopy and droplet characterization. Inelastic scattered light from the trapped droplet was collected using the setup depicted in Fig. 1a, and Raman spectra were recorded at 1-second intervals on the CCD (PIXIS:100B_eXcelon, Princeton Instruments) of an imaging spectrometer (IsoPlane SCT-320, Princeton Instruments). A representative Raman spectrum of an aqueous proline droplet is shown in Fig. 1b. This spectrum features signals from spontaneous Raman scattering along with sharp peaks corresponding to morphology-dependent resonances (MDRs). The positions of these MDRs were tracked over time (Fig. 1c), enabling accurate retrieval of droplet size and refractive index using the MRFIT code.[32] An example of the retrieved size and refractive index for an aqueous proline droplet undergoing photochemical changes in the optical trap is presented in Fig. 1d.

4.1.4 Investigation of indirect photochemical processes. Before attributing observed changes to the direct absorption of light by the organic molecules (which are typically considered non-absorbing in this spectral region), control experiments were performed to exclude indirect photochemical pathways.

First, the potential for oxidation of organic solutes by ozone or oxygen-derived radicals was investigated. Exposure to ozone in solution can degrade amino acids and sugars, often leading to the formation of carbon dioxide or ammonium ions.[50,51] If ozone formation or the presence of other oxygen radicals were

significant, the oxidation rate would be expected to increase with higher dissolved oxygen concentrations.[52] Therefore, experiments were conducted with optically trapped droplets under both purified air and purified nitrogen atmospheres. Fig. S6 illustrates the radius and refractive index profiles for two droplets of similar initial radii, one held in air and the other in nitrogen. The trapping lifetime remained unchanged despite the increased dissolved oxygen concentration in the droplet under air, suggesting that ozone formation and subsequent oxidation are not primary degradation pathways in this system.

Next, the influence of dissolved contaminants acting as potential photosensitizers was evaluated. Iron(III) sulfate ($Fe_2(SO_4)_3$) was selected as a model photosensitizer due to its high aqueous solubility and known ability to form iron-organic complexes that can lead to organic degradation in aerosol droplets.[53] Solutions were prepared by adding the iron salt to 0.5 M glycine solutions to achieve iron concentrations up to 20 mg L^{-1}. Aerosol droplets of these solutions were suspended in the optical trap, and their trapping lifetimes were measured. No significant change in trapping lifetime was observed for droplets containing up to 20 mg L^{-1} of dissolved iron sulfate. Furthermore, as experiments investigating the direct photochemistry of the organic solutes were typically conducted under a nitrogen atmosphere (minimizing dissolved oxygen required for some iron-catalyzed radical formation pathways), and given the observed decrease in the primary photochemical reaction rate with decreasing organic solute concentration (Fig. 5), a photodegradation mechanism dominated by trace iron contaminants is considered unlikely.[54]

Recent work has demonstrated the potential for nucleation to be initiated by high-energy laser pulses through non-photochemical pathways in supersaturated organic/water mixtures.[55] Therefore, we briefly consider the possibility of non-photochemical laser-induced nucleation (NPLIN) occurring in our experiments. Supersaturated glycine solutions have been investigated extensively in the literature, and the experimental conditions have been summarized by Korede *et al.*[56] The peak laser intensities required to initiate crystallization for supersaturated glycine solutions was 240 MW cm^{-2}, an order of magnitude higher than the intensities used in the optical trapping experiments reported here.[57] Additionally, Fig. S1 demonstrates that inorganic aqueous droplets can be suspended indefinitely despite requiring lower laser intensities to initiate NPLIN.[58] The observed changes in the Raman spectra of proline, glucose, ribose, and deoxyribose droplets in Fig. S3 and S4 suggest that a chemical transformation leading to the formation of insoluble products is responsible for water loss and nucleation.

4.2 Determination of concentrations

In the experiments performed here, single droplets are held in a RH controlled cell. Both droplet radius, r, and the real part of the refractive index, n, can be measured with high accuracy as discussed in Section 4.1. In this section, we will outline the methodology to determine droplet composition from measurements of n.

An aqueous droplet with no volatile solutes will reach equilibrium with its surrounding RH when S = RH/100%, where S is the equilibrium water vapor saturation ratio over the droplet. Köhler theory describes the relationship between droplet size and S. One form of the Köhler equation is

$$S = a_w \exp\left(\frac{2\sigma M_w}{r\rho_w RT}\right), \quad (5)$$

where a_w is the water activity of the droplet, σ is the surface tension of the droplet, M_w is the molar mass of water, ρ_w is the density of water, R is the universal gas constant, and T is the temperature.

The exponential function in eqn (5) describes the Kelvin effect and, as we will be dealing with micron-sized droplets (small radius of curvature) at subsaturated RH, it will be negligible. Therefore, it will be set to one in our subsequent analysis and eqn (5) becomes $S = a_w$ and only the solute effect (where the vapor pressure is reduced by dissolved solutes) is important. For an ideal solution, a_w is simply the mole fraction of water. However, the assumption of an ideal solution is not valid for the high solute concentrations found in the droplets studied here.

One approach to account for thermodynamic non-ideality is to parameterize the water activity as a function of the hygroscopicity parameter, κ, through the equation[59]

$$\frac{1}{a_w} = 1 + \kappa\frac{V_{dry}}{V_w}, \quad (6)$$

where V_{dry} is the volume of the dry particle and V_w is the volume of water in the particle. The resulting κ-Köhler theory simplifies water activity calculations in eqn (5). Values for the hygroscopicity parameter range from $\kappa = 0$ (the species does not absorb water and there is no hygroscopic growth) to $\kappa = 1.4$ (the species is very hygroscopic and there is significant hygroscopic growth). As discussed above, we will neglect the Kelvin effect and eqn (5) can then be written as

$$S = \frac{V - V_{dry}}{V - V_{dry}(1-\kappa)}, \quad (7)$$

where the total droplet volume is $V = V_w + V_{dry}$.

Of interest here are aqueous droplets with two solutes: species A and its photoproduct B. For this system, we will have $V_{dry} = V_A + V_B$. To determine κ when multiple solutes are present in an aqueous droplet, the mixing rule[59]

$$\kappa = \sum_j \varepsilon_j \kappa_j \quad (8)$$

can be applied, where for solute j with a volume V_j, $\varepsilon_j = V_j/V_{dry}$ and κ_j is its hygroscopicity parameter. In all experiments performed here, it is observed that as the reaction proceeds, the droplet size decreases partially due to water loss. Therefore, it is reasonable to assume that the hygroscopicity of B is much lower than that of A and can be neglected ($\kappa_B = 0$). Then, $\kappa = \kappa_A V_A/(V_A + V_B)$. Application of this result to eqn (7), along with the definitions for V and V_{dry} given above, yields the following two relations between the volume fraction of A (f_A), the volume

fraction of water (f_w), and the volume fraction of B (f_B) in the droplet:

$$f_w = \frac{S\kappa_A}{S-1} f_A \quad \text{and} \quad f_B = 1 + \frac{1 - S(1-\kappa_A)}{S-1} f_A. \tag{9}$$

As expected, these definitions satisfy $\sum_j f_j = 1$. The relationship between volume fraction and concentration is given by $f_j = M_j c_j \bar{v}_j / N_A$ where, for species j, M_j is the molar mass, c_j is the molecular concentration (molecular number density), $\bar{v}_j$ is the partial specific volume, and N_A is the Avogadro constant. From eqn (9), the relationships between the concentrations will be

$$\begin{aligned} c_w &= \frac{S\kappa_A}{S-1} \frac{M_A \bar{v}_A}{M_w \bar{v}_w} c_A \quad \text{and} \\ c_B &= \frac{N_A}{M_B \bar{v}_B} + \frac{1 - S(1-\kappa_A)}{S-1} \frac{M_A \bar{v}_A}{M_B \bar{v}_B} c_A. \end{aligned} \tag{10}$$

The Clausius–Mossotti relation connects the sum of polarizabilities of all the species present in the solution to the macroscopic dielectric function of the solution, ε. When the imaginary part of the refractive index is zero then $\varepsilon = n^2$ and the Clausius–Mossotti equation can be written as[43]

$$\bar{\alpha} \equiv \frac{n^2 - 1}{n^2 + 2} = \sum_j \bar{\alpha}_j, \tag{11}$$

where $\bar{\alpha}$ is the normalized polarizability of the solution, which is calculated from refractive index measurements. For each species j with a molecular polarizability α_j, the normalized polarizability is defined as $\bar{\alpha}_j = c_j \alpha_j / (3\varepsilon_0)$, where ε_0 is the permittivity of free space.

Inserting eqn (10) into eqn (11) allows the concentration of species A to be expressed as

$$c_A = \frac{M_w (S-1) \bar{v}_w (3\varepsilon_0 \bar{\alpha} M_B \bar{v}_B - N_A \alpha_B)}{M_A M_w \bar{v}_A \bar{v}_w \alpha_B (1 + S(\kappa_A - 1)) + M_B \bar{v}_B (M_w (S-1) \bar{v}_w \alpha_A - M_A S \bar{v}_A \alpha_w \kappa_A)}. \tag{12}$$

In this study, $\bar{\alpha}$ is calculated using measurements of n and eqn (11), with S experimentally controlled. All other terms are either physical constants or known physical parameters or can be reasonably approximated. For the latter assumption, in eqn (12), we set $M_B = M_A$, $\bar{v}_B = \bar{v}_A$, and $\alpha_B = \alpha_A$. All constants and parameters used in the evaluation of eqn (12) are listed in Table S1.

4.3 Analysis of photochemical model

Here, we consider two models: (1) photochemical reactions occur throughout the entire droplet, and (2) photochemical reactions are restricted to a thin interfacial region at the droplet surface. In both cases, reactions are kinetically controlled with no diffusion limitation (*e.g.*, in the surface-only model, reactants rapidly diffuse from the droplet interior to the surface).

The rate of formation of the excited state A*, represented by its concentration c_{A^*}, from reactions (1a)–(1e) is

$$\frac{dc_{A^*}}{dt} = \sigma_A I c_A - k_{ex1} c_{A^*} - k_1 c_{A^*} - k_{ex2} c_{A^*} c_B - k_2 c_{A^*} c_B. \tag{13}$$

Integrating both sides over droplet volume, V, yields

$$\frac{dc_{A^*}}{dt} = \frac{1}{V} \int \sigma_A I c_A dV - (k_{ex1} + k_1 + k_{ex2} c_B + k_2 c_B) c_{A^*}. \tag{14}$$

The integral on the right-hand side is the power absorbed by the droplet, W_{abs}, and is related to the absorption cross-section, C_{abs}, of the droplet through[30]

$$W_{abs} = I_0 C_{abs} = h\nu \int \sigma_A I c_A dV, \tag{15}$$

where h is Planck's constant, ν is the frequency of the excitation light source, and I_0 is the peak intensity (irradiance) of the light source in radiant flux per area. For a focused Gaussian beam, such as that used in the photochemical experiments here, I_0 is the intensity at its focal point. It can be defined as $I_0 = 2P/\pi {w_0}^2$, where P is the total beam power and w_0 is the beam waist radius.

For a sphere illuminated by a plane wave, optical cross-sections can be determined using Mie theory. Generalized Lorenz–Mie theory (GLMT) extends this framework to arbitrarily shaped beams (*e.g.*, Gaussian beams).[60] The results from these calculations are exact but the equations used are complicated and not explicit in terms of all of the input parameters (for the system here, the concentration of the absorber c_A, droplet size, and beam waist). However, it is possible to make these dependencies explicit using the less accurate approach of geometric optics. If we first consider a weakly absorbing sphere illuminated by a plane wave, geometric optics yields an absorption cross-section, C_{abs}^{pw}, that is proportional to the volume of the sphere.[61] This approximation can be simplified with the further assumption that the real part of the refractive index n of the sphere can be set to 1, leading to the intuitive expression

$$C_{abs}^{pw} \simeq \frac{4}{3} \pi r^3 \sigma_A c_A, \tag{16}$$

where we have applied $k = \sigma_A c_A \lambda / 4\pi$, which relates the imaginary part of the refractive index, k, to the concentration of the sole absorbing species in solution, A. This result aligns with the perhaps naive expectation that the absorption cross-section should scale with the volume of the sphere and the number of absorbing molecules per unit volume. Fig. S13 compares results from eqn (16) to Mie theory calculations for weakly absorbing spheres. Aside from the absence of Mie resonances, the simple equation predicts C_{abs}^{pw} with moderate accuracy. More importantly, it gives the proper scaling for the size and concentration dependent behaviour.

The absorption cross-section for a weakly absorbing sphere centred on the focal point of a Gaussian beam, C_{abs}^{G}, can be approximated in a similar manner to yield

$$C_{abs}^{G} \simeq \frac{{w_0}^2}{2r^2}\left(1 - e^{-2r^2/{w_0}^2}\right) C_{abs}^{pw} = \frac{2}{3}\pi r \sigma_A c_A {w_0}^2 \left(1 - e^{-2r^2/{w_0}^2}\right). \quad (17)$$

Fig. S14 compares results from eqn (17) to GLMT calculations. Inaccuracies similar to those discussed above for eqn (16) are observed, however the correct scaling in terms of the parameters c_A, r, and w_0 is observed. In particular, once $r \gg w_0$ then C_{abs}^{G} scales with radius rather than volume like C_{abs}^{pw}.

Application of eqn (15) and (17) to eqn (14), and assuming that r is larger enough compared to w_0 so that the term $1 - e^{-2r^2/w_0^2} \sim 1$ results in

$$\frac{dc_{A^*}}{dt} = \frac{\sigma_A \Phi}{\pi r^2} c_A - (k_{ex1} + k_1 + k_{ex2} c_B + k_2 c_B) c_{A^*}, \quad (18)$$

where $\Phi = P/h\nu$ represents the total photon rate of the beam.

Applying the steady-state approximation, $dc_{A^*}/dt = 0$, to eqn (18) then gives

$$c_{A^*} = \frac{\gamma c_A}{k_1 + k_{ex1} + (k_2 + k_{ex2}) c_B}, \quad (19)$$

where $\gamma = \sigma_A \Phi/\pi r^2$.

From reaction (1a), (1b), and (1d) the rate of change of species A can be expressed as

$$\frac{dc_A}{dt} = -\gamma c_A + k_{ex1} c_{A^*} + k_{ex2} c_{A^*} c_B, \quad (20)$$

which, using eqn (19), can be written as

$$\frac{dc_A}{dt} = -\gamma c_A \frac{k_1 + k_2 (c_{A_0} - c_A)}{k_1 + k_{ex1} + (k_2 + k_{ex2})(c_{A_0} - c_A)}, \quad (21)$$

where, at $t = 0$, $c_A = c_{A_0}$ and $c_B = 0$, and we set $c_B = c_{A_0} - c_A$.

Eqn (21) is a non-linear ordinary differential equation that can be solved using numerical methods (*e.g.*, the commonly used fourth-order Runge–Kutta method). However, if we assume that $k_1 + k_{ex1} \gg (k_2 + k_{ex2})(c_{A_0} - c_A)$ then eqn (21) becomes

$$\frac{dc_A}{dt} = -\gamma \phi_1 c_A - \gamma \phi_2 c_A (c_{A_0} - c_A), \quad (22)$$

where $\phi_1 = k_1/(k_1 + k_{ex1})$ and $\phi_2 = k_2/(k_1 + k_{ex1})$. These are the effective quantum yields for the photochemical pathways.[33]

Eqn (22) can be integrated to yield

$$c_A = c_{A_0} \frac{\phi_1 + \phi_2 c_{A_0}}{\phi_2 c_{A_0} + \phi_1 \exp\left[\gamma(\phi_1 + \phi_2 c_{A_0}) t\right]}. \quad (23)$$

Finally, by assuming that $\phi_1/(\phi_2 c_{A_0}) \ll 1$, eqn (23) can be rewritten as a slightly more compact sigmoid function that is given in eqn (2) with two parameters β and t_0, which are defined in eqn (3). The form in eqn (2) is of practical use when fitting kinetic data.

For the case where photochemistry occurs solely at the droplet surface, the above approach can be modified by considering that absorption only occurs within a thin interfacial layer at the droplet surface. This involves replacing eqn (16) with

$$C_{abs}^{pw} \simeq 4\pi r^2 \delta \sigma_A c_A, \quad (24)$$

where δ is the thickness of the reactive interfacial shell. This expression is an approximation derived from geometric optics for the plane wave illumination of a weakly absorbing spherical shell in the regime where the shell thickness is significantly smaller than the droplet radius ($\delta \ll r$). The core is non-absorbing in this model. Fig. S15 compares absorption calculations from GLMT to simpler geometric optics calculations for a weakly absorbing shell illuminated by a focused Gaussian beam. As with the earlier comparison for the homogeneous weakly absorbing sphere, the correct scaling with respect to beam and particle parameters is observed.

After replacing eqn (16) with eqn (24), the analysis then proceeds as before, resulting in γ in eqn (19) being defined as $\gamma = 3\delta\sigma_A\Phi/\pi r^3$, and the parameters β and t_0 in eqn (2) are defined in eqn (4).

Conflicts of interest

There are no conflicts to declare.

Data availability

All data supporting the findings of this study are available within the article and its supplementary information (SI). Supplementary information is available. See DOI: https://doi.org/10.1039/d5cp03615a.

Additional raw datasets and code are available from the corresponding author upon reasonable request.

Acknowledgements

This work is supported by the Alfred P. Sloan Foundation (Grant Number: G-2024-22579).

References

1 C. George, M. Ammann, B. D'Anna, D. Donaldson and S. A. Nizkorodov, Heterogeneous photochemistry in the atmosphere, *Chem. Rev.*, 2015, **115**, 4218–4258.
2 N. J. Green, J. Xu and J. D. Sutherland, Illuminating life's origins: UV photochemistry in abiotic synthesis of biomolecules, *J. Am. Chem. Soc.*, 2021, **143**, 7219–7236.
3 B. J. Finlayson-Pitts and J. N. Pitts, Photochemistry of Important Atmospheric Species, *Chemistry of the Upper and Lower Atmosphere*, Academic Press, San Diego, 2000, pp. 86–129.
4 C. George, B. D'Anna, H. Herrmann, C. Weller, V. Vaida, D. J. Donaldson, T. Bartels-Rausch and M. Ammann, Emerging areas in atmospheric photochemistry, in *Atmospheric and Aerosol Chemistry, Topics in Current Chemistry*, ed. V. F. McNeill and P. A. Ariya, Springer, Berlin, Heidelberg, 2014, vol. 339, pp. 1–53.

5 B. H. Patel, C. Percivalle, D. J. Ritson, C. D. Duffy and J. D. Sutherland, Common origins of rna, protein and lipid precursors in a cyanosulfidic protometabolism, *Nat. Chem.*, 2015, **7**, 301–307.
6 D. J. Ritson and J. D. Sutherland, Thiophosphate photochemistry enables prebiotic access to sugars and terpenoid precursors, *Nat. Chem.*, 2023, **15**, 1470–1477.
7 C. M. Dobson, G. B. Ellison, A. F. Tuck and V. Vaida, Atmospheric aerosols as prebiotic chemical reactors, *Proc. Natl. Acad. Sci. U. S. A.*, 2000, **97**, 11864–11868.
8 I. Nam, H. G. Nam and R. N. Zare, Abiotic synthesis of purine and pyrimidine ribonucleosides in aqueous microdroplets, *Proc. Natl. Acad. Sci. U. S. A.*, 2018, **115**, 36–40.
9 A. Castañeda, Z. Li, T. Joo, K. Benham, B. Burcar, R. Krishnamurthy, C. Liotta, N. Ng and T. Orlando, Prebiotic phosphorylation of uridine using diamidophosphate in aerosols, *Sci. Rep.*, 2019, **9**, 13527.
10 A. M. Deal, R. J. Rapf and V. Vaida, Water-air interfaces as environments to address the water paradox in prebiotic chemistry: A physical chemistry perspective, *J. Phys. Chem. A*, 2021, **125**, 4929–4942.
11 D. T. Holden, N. M. Morato and R. G. Cooks, Aqueous microdroplets enable abiotic synthesis and chain extension of unique peptide isomers from free amino acids, *Proc. Natl. Acad. Sci. U. S. A.*, 2022, **119**, e2212642119.
12 A. Ianeselli, A. Salditt, C. Mast, B. Ercolano, C. L. Kufner, B. Scheu and D. Braun, Physical non-equilibria for prebiotic nucleic acid chemistry, *Nat. Rev. Phys.*, 2023, **5**, 185–195.
13 I. Nam, J. K. Lee, H. G. Nam and R. N. Zare, Abiotic production of sugar phosphates and uridine ribonucleoside in aqueous microdroplets, *Proc. Natl. Acad. Sci. U. S. A.*, 2017, **114**, 12396–12400.
14 W. Wang, L. Qiao, J. He, Y. Ju, K. Yu, G. Kan, C. Guo, H. Zhang and J. Jiang, Water microdroplets allow spontaneously abiotic production of peptides, *J. Phys. Chem. Lett.*, 2021, **12**, 5774–5780.
15 M. I. Jacobs, R. D. Davis, R. J. Rapf and K. R. Wilson, Studying chemistry in micro-compartments by separating droplet generation from ionization, *J. Am. Soc. Mass Spectrom.*, 2018, **30**, 339–343.
16 E. A. Parmentier, G. David, P. C. Arroyo, S. Bibawi, K. Esat and R. Signorell, Photochemistry of single optically trapped oleic acid droplets, *J. Aerosol Sci.*, 2021, **151**, 105660.
17 E. A. Parmentier, P. Corral Arroyo, R. Gruseck, L. Ban, G. David and R. Signorell, Charge effects on the photodegradation of single optically trapped oleic acid aerosol droplets, *J. Phys. Chem. A*, 2022, **126**, 4456–4464.
18 S. Ishizuka, O. Reich, G. David and R. Signorell, Photoinduced shrinking of aqueous glycine aerosol droplets, *Atmos. Chem. Phys.*, 2023, **23**, 5393–5402.
19 J. K. Lee, S. Banerjee, H. G. Nam and R. N. Zare, Acceleration of reaction in charged microdroplets, *Q. Rev. Biophys.*, 2015, **48**, 437–444.
20 Z. Wei, Y. Li, R. G. Cooks and X. Yan, Accelerated reaction kinetics in microdroplets: Overview and recent developments, *Annu. Rev. Phys. Chem.*, 2020, **71**, 31–51.
21 M. F. Ruiz-López and M. T. C. Martins-Costa, Disentangling reaction rate acceleration in microdroplets, *Phys. Chem. Chem. Phys.*, 2022, **24**, 29700–29704.
22 K. R. Wilson and A. M. Prophet, Chemical kinetics in microdroplets, *Annu. Rev. Phys. Chem.*, 2024, **75**, 185–208.
23 G. Rovelli, M. I. Jacobs, M. D. Willis, R. J. Rapf, A. M. Prophet and K. R. Wilson, A critical analysis of electrospray techniques for the determination of accelerated rates and mechanisms of chemical reactions in droplets, *Chem. Sci.*, 2020, **11**, 13026–13043.
24 K. Gong, A. Nandy, Z. Song, Q.-S. Li, A. Hassanali, G. Cassone, S. Banerjee and J. Xie, Revisiting the enhanced chemical reactivity in water microdroplets: The case of a Diels-Alder reaction, *J. Am. Chem. Soc.*, 2024, **146**, 31585–31596.
25 H.-M. Tzeng, K. F. Wall, M. Long and R. Chang, Laser emission from individual droplets at wavelengths corresponding to morphology-dependent resonances, *Opt. Lett.*, 1984, **9**, 499–501.
26 J. B. Snow, S.-X. Qian and R. K. Chang, Stimulated Raman scattering from individual water and ethanol droplets at morphology-dependent resonances, *Opt. Lett.*, 1985, **10**, 37–39.
27 J. D. Eversole, H.-B. Lin, A. L. Huston, A. J. Campillo, P. T. Leung, S. Liu and K. Young, High-precision identification of morphology-dependent resonances in optical processes in microdroplets, *J. Opt. Soc. Am. B*, 1993, **10**, 1955–1968.
28 P. Corral Arroyo, G. David, P. A. Alpert, E. A. Parmentier, M. Ammann and R. Signorell, Amplification of light within aerosol particles accelerates in-particle photochemistry, *Science*, 2022, **376**, 293–296.
29 A. Rafferty, B. Vennes, A. Bain and T. C. Preston, Optical trapping and light scattering in atmospheric aerosol science, *Phys. Chem. Chem. Phys.*, 2023, **25**, 7066–7089.
30 J. W. Cremer, K. M. Thaler, C. Haisch and R. Signorell, Photoacoustics of single laser-trapped nanodroplets for the direct observation of nanofocusing in aerosol photokinetics, *Nat. Commun.*, 2016, **7**, 10941.
31 A. Logozzo, B. Vennes, R. Kaur Kohli, J. F. Davies, D. J. Castillo-Pazos, C.-J. Li, C. D. Neish and T. C. Preston, Photochemically driven peptide formation in supersaturated aerosol droplets, *Angew. Chem., Int. Ed.*, 2023, e202409788.
32 T. C. Preston and J. P. Reid, Determining the size and refractive index of microspheres using the mode assignments from Mie resonances, *J. Opt. Soc. Am. A*, 2015, **32**, 2210–2217.
33 F. Tong, M. P. Hanson and C. J. Bardeen, Analysis of reaction kinetics in the photomechanical molecular crystal 9-methylanthracene using an extended Finke–Watzky model, *Phys. Chem. Chem. Phys.*, 2016, **18**, 31936–31945.
34 M. A. Watzky and R. G. Finke, Transition metal nanocluster formation kinetic and mechanistic studies. a new mechanism when hydrogen is the reductant: slow, continuous nucleation and fast autocatalytic surface growth, *J. Am. Chem. Soc.*, 1997, **119**, 10382–10400.
35 L. Bentea, M. A. Watzky and R. G. Finke, Sigmoidal Nucleation and Growth Curves Across Nature Fit by the Finke–Watzky Model of Slow Continuous Nucleation and

Autocatalytic Growth: Explicit Formulas for the Lag and Growth Times Plus Other Key Insights, *J. Phys. Chem. C*, 2017, **121**, 5302–5312.
36 J. R. Lakowicz, *Principles of fluorescence spectroscopy*, Springer, 3rd edn, 2006.
37 G. O. Phillips and T. Rickards, Photodegradation of carbohydrates. part iv. direct photolysis of d-glucose in aqueous solution, *J. Chem. Soc. B*, 1969, 455–461.
38 D. Tuna, A. L. Sobolewski and W. Domcke, Electronically excited states and photochemical reaction mechanisms of β-glucose, *Phys. Chem. Chem. Phys.*, 2014, **16**, 38–47.
39 K. N. Rowell, S. H. Kable and M. J. T. Jordan, An assessment of the tropospherically accessible photo-initiated ground state chemistry of organic carbonyls, *Atmos. Chem. Phys.*, 2022, **22**, 929–949.
40 M. Kasha, H. R. Rawls and M. A. El-Bayoumi, The exciton model in molecular spectroscopy, *Pure Appl. Chem.*, 1965, **11**, 371–392.
41 F. Würthner, T. E. Kaiser and C. R. Saha-Möller, J-aggregates: From serendipitous discovery to supramolecular engineering of functional dye materials, *Angew. Chem., Int. Ed.*, 2011, **50**, 3376–3410.
42 N. J. Hestand and F. C. Spano, Expanded theory of h- and j-molecular aggregates: The effects of vibronic coupling and intermolecular charge transfer, *Chem. Rev.*, 2018, **118**, 7069–7163.
43 B. Auguié and E. C. Le Ru, Optical absorption of dye molecules in a spherical shell geometry, *J. Phys. Chem. C*, 2018, **122**, 19110–19115.
44 A. Djorović, M. Meyer, B. L. Darby and E. C. Le Ru, Accurate modeling of the polarizability of dyes for electromagnetic calculations, *ACS Omega*, 2017, **2**, 1804–1811.
45 T. Goto, A. Ikehata, Y. Morisawa and Y. Ozaki, Electronic transitions of protonated and deprotonated amino acids in aqueous solution in the region 145–300 nm studied by attenuated total reflection far-ultraviolet spectroscopy, *J. Phys. Chem. A*, 2013, **117**, 2517–2528.
46 A. Rafferty and T. C. Preston, Measuring the size and complex refractive index of an aqueous aerosol particle using electromagnetic heating and cavity-enhanced Raman scattering, *Phys. Chem. Chem. Phys.*, 2018, **20**, 17038–17047.
47 A. Bain, A. Rafferty and T. C. Preston, The wavelength-dependent complex refractive index of hygroscopic aerosol particles and other aqueous media: An effective oscillator model, *Geophys. Res. Lett.*, 2019, **46**, 10636–10645.
48 A. Logozzo and T. C. Preston, Temperature-controlled dual-beam optical trap for single particle studies of organic aerosol, *J. Phys. Chem. A*, 2021, **126**, 109–118.
49 A. Rafferty and T. C. Preston, Trapping positions in a dual-beam optical trap, *J. Appl. Phys.*, 2021, **130**, 183105.
50 V. K. Sharma and N. J. Graham, Oxidation of amino acids, peptides and proteins by ozone: a review, *Ozone: Sci. Eng.*, 2010, **32**, 81–90.
51 Z. Wang, C. Chen, W. Ma and J. Zhao, Photochemical coupling of iron redox reactions and transformation of low-molecular-weight organic matter, *J. Phys. Chem. Lett.*, 2012, **3**, 2044–2051.
52 P. A. Alpert, J. Dou, P. Corral Arroyo, F. Schneider, J. Xto, B. Luo, T. Peter, T. Huthwelker, C. N. Borca and K. D. Henzler, *et al.*, Photolytic radical persistence due to anoxia in viscous aerosol particles, *Nat. Commun.*, 2021, **12**, 1769.
53 G. R. Wentworth and H. A. Al-Abadleh, Drifts studies on the photosensitized transformation of gallic acid by iron (iii) chloride as a model for hulis in atmospheric aerosols, *Phys. Chem. Chem. Phys.*, 2011, **13**, 6507–6516.
54 J. Dou, P. A. Alpert, P. Corral Arroyo, B. Luo, F. Schneider, J. Xto, T. Huthwelker, C. N. Borca, K. D. Henzler, J. Raabe, B. Watts, H. Herrmann, T. Peter, M. Ammann and U. K. Krieger, Photochemical degradation of iron(III)-citrate/citric acid aerosol quantified with the combination of three complementary experimental techniques and a kinetic process model, *Atmos. Chem. Phys.*, 2021, **21**, 315–338.
55 B. Garetz, J. Aber, N. Goddard, R. Young and A. Myerson, Nonphotochemical, polarization-dependent, laser-induced nucleation in supersaturated aqueous urea solutions, *Phys. Rev. Lett.*, 1996, **77**, 3475.
56 V. Korede, N. Nagalingam, F. M. Penha, N. van der Linden, J. T. Padding, R. Hartkamp and H. B. Eral, A review of laser-induced crystallization from solution, *Cryst. Growth Des.*, 2023, **23**, 3873–3916.
57 X. Sun, B. A. Garetz and A. S. Myerson, Supersaturation and polarization dependence of polymorph control in the non-photochemical laser-induced nucleation (nplin) of aqueous glycine solutions, *Cryst. Growth Des.*, 2006, **6**, 684–689.
58 K. Fang, S. Arnold and B. A. Garetz, Nonphotochemical laser-induced nucleation in levitated supersaturated aqueous potassium chloride microdroplets, *Cryst. Growth Des.*, 2014, **14**, 2685–2688.
59 M. Petters and S. Kreidenweis, A single parameter representation of hygroscopic growth and cloud condensation nucleus activity, *Atmos. Chem. Phys.*, 2007, **7**, 1961–1971.
60 G. Gouesbet, J. Lock and G. Gréhan, Generalized Lorenz–Mie theories and description of electromagnetic arbitrary shaped beams: localized approximations and localized beam models, a review, *J. Quant. Spectrosc. Radiat. Transfer*, 2011, **112**, 1–27.
61 C. F. Bohren and D. R. Huffman, *Absorption and scattering of light by small particles*, John Wiley & Sons, 2008.